Probing the light harvesting and charge rectification of bismuth nanoparticles behind the promoted photoreactivity onto Bi/BiOCl catalyst by (in-situ) electron microscopy

Xiaofeng Chang [a,1], Lin Xie [a,1], Wei E.I. Sha [b,1], Kun Lu [c], Qi Qi [d], Chenyu Dong [a], Xingxu Yan [a], Mohammed A. Gondal [e], Siddique G. Rashid [f], Qi I. Dai [g], Wen Zhang [d], Longqi Yang [a], Xingdu Qiao [a], Liang Mao [c], Peng Wang [a,*]

[a] National Laboratory of Solid State Microstructures, College of Engineering and Applied Sciences and Collaborative Innovation Center of Advanced Microstructures, Nanjing University, Nanjing 210093, China
[b] Department of Electrical and Electronic Engineering, University of Hong Kong, Pokfulam Road, Hong Kong
[c] State Key Laboratory of Pollution Control and Resource Reuse, School of The Environment, Nanjing University, Nanjing 210093, China
[d] School of Chemistry and Chemical Engineering, Southeast University, Nanjing 211189, China
[e] Physics Department and Center of Excellence in Nanotechnology, King Fahd University of Petroleum and Minerals, Dhahran 31261, Saudi Arabia
[f] School of Chemistry and Molecular Biosciences, University of Queensland, Brisbane, QLD 4067, Australia
[g] Department of Electrical and Computer Engineering, University of Illinois at Urbana-Champaign, Urbana, IL, USA

ARTICLE INFO

ABSTRACT

State-of-the-art electron microscopy has enabled us to investigate microstructural details down to sub-subångström and milli-electron-volt resolution level. The enhanced photoreactivity over bismuth hybridized BiOCl catalyst (Bi/BiOCl) has been reported recently, however, the mechanistic understandings of this improved photoreactivity especially the optical behavior of bismuth nanoparticles (Bi NPs) are still obscured and in debate. The optical absorption features of Bi NPs and the charge transfer characteristic between bismuth and BiOCl have been considered as the major physicochemical origin for the promoted photoreactivity. Based on the advanced (in-situ) electron microscopy of monochromated electron energy loss spectroscopy in scanning transmission electron microscopy imaging mode (Mono-STEM-EELS) along with related theoretical investigations, in this work, we for the first time distinguished and explained the optical absorption originated from the localized surface plasmon resonances (LSPR) effect and direct band gap transition in an individual bismuth nanoparticle as well as transportation of photogenerated carriers at the interface of Bi/BiOCl. These findings could provide better understandings about the origin of the improved photoreactivity of various bismuth-hybridized photocatalysts.

© 2016 Elsevier B.V. All rights reserved.

1. Introduction

Since the pioneer achievements in 2001 for the development of visible light driven photocatalysts, the quest to synthesize visible-light-activated photocatalysts with suitable band positions, high mobility of charge carriers and appropriate surfaces for required reactions has attracted intense research in this field [1–4]. TiO$_2$ has been extensively accepted as an efficient, stable and low-cost photocatalyst since 1972. However, its larger band gap (E$_g$ = 3.2 eV for anatase, 3.0 eV for rutile phase) restricts its effective use under visible light irradiations, which are large fraction of the abundant solar flux [5–8]. It has been gradually realized that the photocatalytic efficiency is more likely associated with the charge transfer kinetics. Bismuth is a semi-metallic material that has slight overlap between the bottom of the conduction band (CB) and the top of the valence band (VB) in the bulk phase (38 meV at 5 K). The semimetal-to-semiconductor transition in bismuth has been reported by decreasing its size to nanoscale due to the quantum confinement effect [9].

Ever since the first report on the localized surface plasmon resonance (LSPR) band simulation of bismuth nanoparticles (Bi NPs) on the basis of Mie theory in early 1996, the LSPR effect of
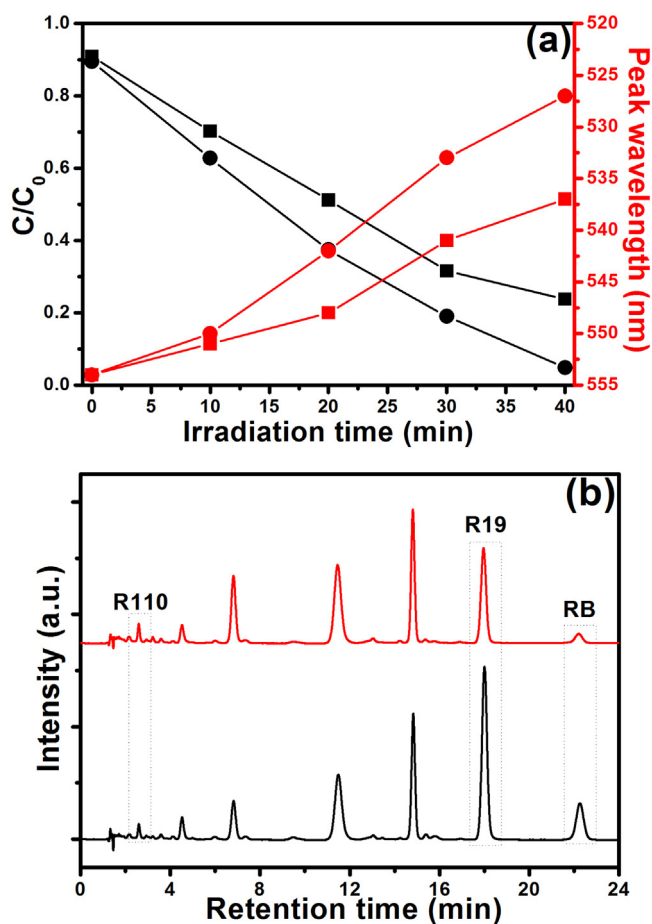
Fig. 1. (a) Variations of RB concentration and characteristic absorption band wavelength of RB solution over pristine BiOCl (square) and Bi/BiOCl catalyst (circle) as a function of visible light irradiation time. (b) HPLC chromatograms of the degradation intermediates in the presence of pristine BiOCl (black) and Bi/BiOCl catalyst (red) after 40 min. Experimental conditions: catalyst dosage = 50 mg, initial concentration of RB = 12 mg L^{-1}, volume of RB aq. = 200 mL. (For interpretation of the references to colour in this figure legend, the reader is referred to the web version of this article.)

reported by Dong and Sun's studies [18,22]. Recently, Zhao et al. also see the visible light absorption of Bi NPs as a consequence of indirect allowed transition [16].

Apart from the dispute of LSPR band position, still there is no generally accepted conclusion on the charge transfer between bismuth and main photocatalyst. For instance, it has been considered that the photogenerated electrons from BiOX (X = Cl, Br, I) CB inject into Bi NPs to create an interfacial charge equilibrium that facilitates the photogenerated electron-induced multistep reduction of O_2 and the photocatalytic efficiency [19–21]. However, contradictory results have also been reported in a recent research carried out by Dong and Sun et al., indicating visible light excited electrons from Bi NPs transferred to the CB of BiOCl [18,22]. Recently, Feng et al. also reported the highly efficient photoreactivity over a newly designed ternary photocatalytic system of Bi/BiOCl/BiVO$_4$, and stated that a charge transfer from the surface plasmonic bismuth to the CB edge of BiVO$_4$ may take place under visible light irradiation as well [24].

Over the past decades, state-of-the-art electron microscopy has revolutionized our understanding of materials by revealing the crystal and electronic structural details down to sub-atomic and milli-electron-volt resolution [25–27]. In this regard, the work presented here begins with the evaluation of enhanced photodegradation onto a model composite photocatalyst of Bi/BiOCl synthesized by photoreduction method. Subsequently, the optical absorption caused by LSPR effect and direct band gap of single bismuth nanoparticle that grew in-situ on BiOCl nanosheet under the excitation of inelastic electron beam (e$^-$ beam) in a transmission electron microscope (TEM) has been well distinguished, by using state-of-the-art monochromated electron energy loss spectroscopy in scanning TEM imaging mode (Mono-STEM-EELS) with near atomic spatial resolution, which is also called spatially-resolved valence electron energy loss spectroscopy (VEELS) technique [28]. Furthermore, the charge transfer at the interface of Bi NPs and BiOCl has also been reasonably substantiated as well based on the band structural parameters obtained by Mono-STEM-EELS measurement. Hence the possible mechanism behind improved photoreactivity over Bi/BiOCl catalyst was probed for the first time using our advanced electron microscopy techniques.

2. Experimental

2.1. Materials and preparation

All chemicals used in the study were of reagent grade and applied without further purification. Sodium bismuthate hydrate (NaBiO$_3$·2H$_2$O) and hydrochloric acid (HCl, 37 wt%) were used as reagents supplied by Sinopharm Chemical Reagent Co., Ltd. China. Micro-sized (200 mesh) and nano-sized (40 nm) bismuth particles were purchased from Aladdin Reagents Co., Ltd. China. Model contaminants of Rhodamine B (RB) and methylene blue (MB) were purchased from Tianjin China Chemical Reagent Ltd. Deionized (DI) water with resistance over 15 MΩ cm was used in the whole experiment.

Single crystallized BiOCl nanosheets dominated with {001} facets were synthesized at first for the synthesis of Bi/BiOCl catalyst by e$^-$ beam exposure in a transmission electron microscope [29,30], or by UV-induced photoreduction strategy [17]. In a typical synthesis of Bi/BiOCl catalyst via photoreduction method, 1.5 g of BiOCl was added into 150 mL ammonium oxalate ((NH$_4$)$_2$C$_2$O$_4$, Sinopharm Chemical Reagent Co., Ltd. China) aqueous solution with concentration of 1 g L^{-1} (as hole scavenger). The suspension was illumined by a full-arc Xenon lamp (Beijing Trusttech Co., Ltd., CHF-XM) for 5 min, afterwards the resulting solid products were washed
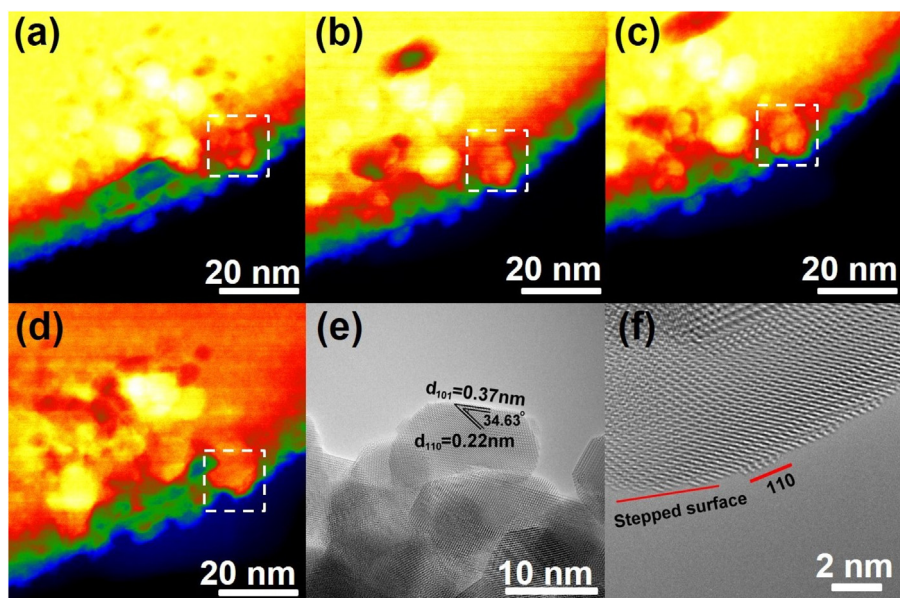
nanostructured bismuth has become hot topic of the research. The dependence of LSPR band on size and shape of Bi NPs from UV to IR has been studied both in theoretical calculations and in experimental investigations [10,11]. A growing number of efforts have also been put forward to exploit the LSPR effect of Bi NPs in UV region for heterogeneous photocatalysis [12–16]. Meanwhile, various bismuth hybridized photocatalytic systems (such as Bi/BiOCl system) with enhanced photoreactivity were developed, where an efficient charge rectification at the interface was achieved by building a heterojunction-like contact between Bi NPs and main photocatalyst [17–22]. However, the detailed mechanism behind the improved photoreactivity on such catalyst is still not well understood. For example, the origin of light harvesting by Bi NPs is still far from being fully understood due to the limited detecting facilities at (near) atomic spatial resolution. Gutiérrez and Wang et al. pointed out that the LSPR band of Bi NPs should be located at UV region (253 nm or 265 nm) [10,14], and Yu et al. suggested that the Bi NPs can only be excited under UV light irradiations in Bi/BiOCl catalysts rather than visible light irradiations [19]. A recent study conducted by Dong et al. also reported the efficient removal of NO and Cr (VI) contaminants under UV or visible light exposure in the presence of nanostructured bismuth [13,16]. However, Velasco-Arias et al. explained that the absorption of Bi NPs (8–20 nm in size) in the UV range could be due to the presence of Bi(III) species in the colloids [23], and the visible light responded LSPR band was further

Fig. 2. HAADF images (in false color) of single-crystalline BiOCl exposed by e⁻ beam (average dose rate: ca. 0.5 e/A² s) for 5 min (a), 10 min (b), 20 min (c) and 40 min (d) respectively. The dashed squares in (a–d) indicate the growth and coalescence of Bi NPs. (e) depicts the HRTEM image of an individual bismuth nanoparticle and (f) shows the aberration-corrected HRTEM image near a (110) surface plane with a stepped surface.
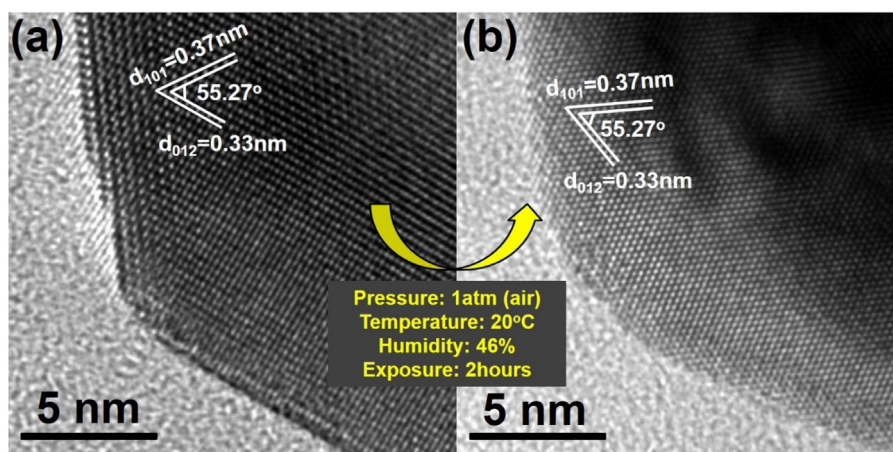

Fig. 3. Ex-situ TEM characterization: HRTEM images of the fresh grown bismuth nanoparticle induced by e⁻ beam irradiation before (a) and after (b) exposing in air (humidity: 46%) at 20 °C for 2 h. The bismuth nanoparticle was slightly tilted possibly owning to the vibration during the extraction and re-loading of sample holder in ex-situ experiment.
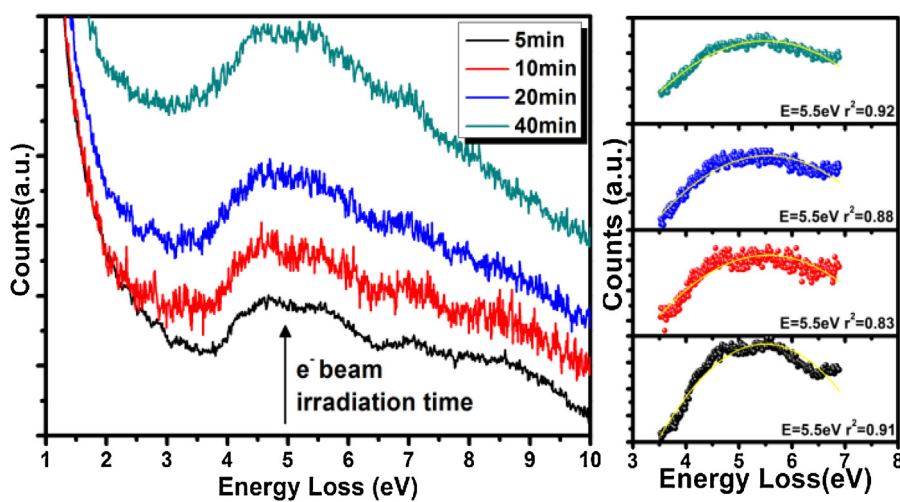

Fig. 4. Temporal evolution of the normalized surface-loss Mono-STEM-EELS acquired with the e⁻ beam passing through the same vacuum position adjacent to the e⁻ beam produced bismuth nanoparticle.
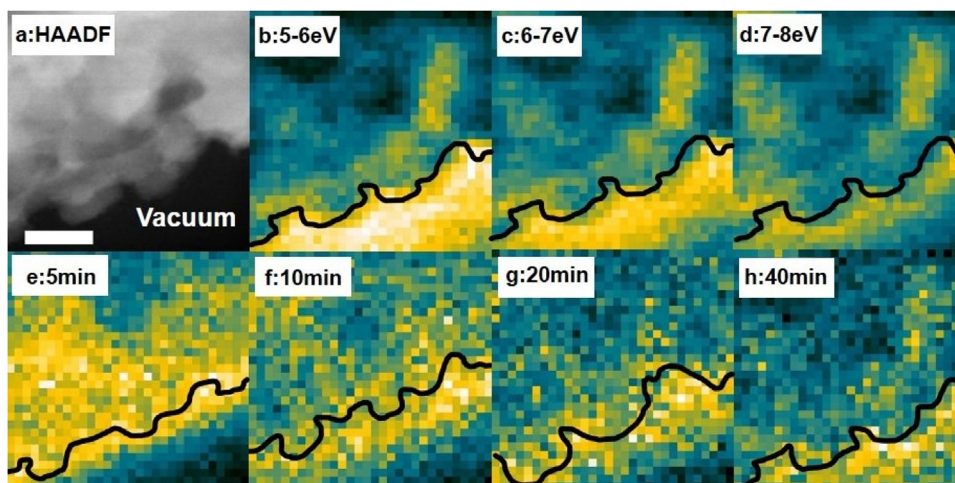
Fig. 5. HAADF image of the single-crystalline BiOCl exposed by e⁻ beam for 40 min (a, scale bar: 10 nm), the corresponding Mono-STEM-EELS maps extracted at different energy regions (b–d), as well as the EELS maps (extracted at 5.5 eV) of the identical specimen region irradiated for different periods (e–h). The solid black lines show contour of the irradiated specimen. The pixel contrasts in both (b–d) and (e–h) have been normalized in order to quantitatively show the optical response. Average e⁻ beam dose rate: ca. 0.5 e/A² s.
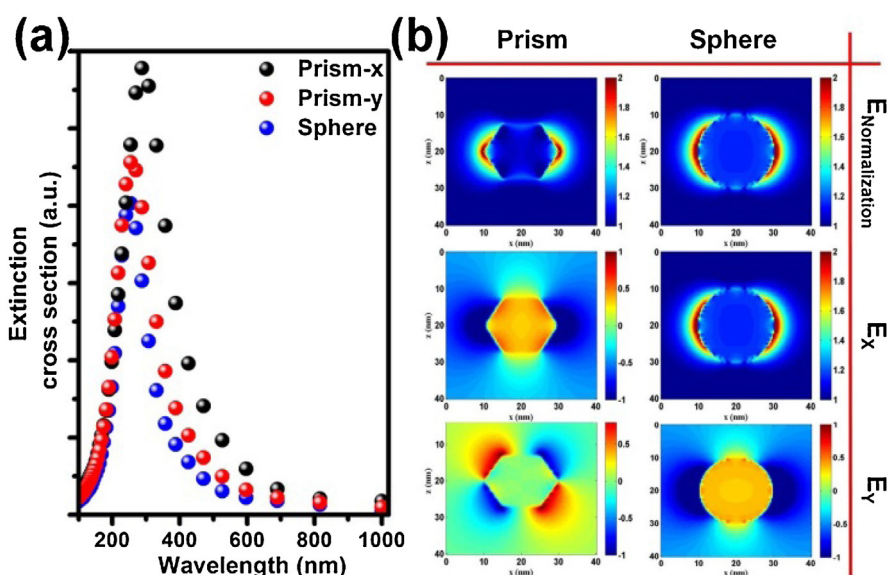

Fig. 6. Simulated extinction cross-section (a) for an individual bismuth nanoparticle with hexagonal prism (edge length = 10 nm, height = 20 nm) and spherical 3D morphology (diameter = 20 nm), and their corresponding electric filed distributions at 5.5 eV (b).

by DI water and absolute ethanol successively, and finally dried in vacuum at 30 °C.

2.2. Photoreactivity evaluation

A Xenon lamp (Beijing Trusttech Co. Ltd., PLS-SXE-300) with power of 300 W was adopted as the source of excitation in the photodegradation experiment, and a broad band-pass light filter (400–800 nm) was equipped to obtain incident visible light. The catalyst was removed by centrifugation (4000 rpm) after photodegradation, and the concentrations of RB and MB in centrifuged aqueous solution were monitored at 554 nm and 664 nm by using a UV–vis spectrophotometer (Hitach U-3900), respectively. The total organic carbon (TOC) was determined by Elemental Vario TOC analyzer. The N-deethylated intermediates were detected by an Alliance 2695 HPLC (Waters) equipped with UV–vis diode array detector using a C18 inversed-phase column (Agilent Eclipse XDB-C18, 150 × 4.6 mm, 5 μm). Ammonium acetate and methanol were

used as mobile phase, and a programmed gradient elution was conducted according to the method reported by Yu et al. [31]. The flow rate was 1.0 mL min⁻¹, and the injection volume was 50 μL.

For liquid chromatography-mass spectrometry (LC–MS) analysis, the supernatant after photodegradation was dried using lyophilizer for 3 days, and then re-dissolved in 1 mL methanol. LC/MS analysis was carried out on a Thermo liquid chromatograph connected to a Thermo LCQ Advantages (Quest LCQ Duo, USA) mass spectrometer through an ESI interface. Separation was performed on a C18 reverse-phase column (150 × 2.1 mm, 5 μm particle, Agilent). Injection volume was 10 μL. The mobile phase was made up of methanol (65%) and water (35%), and eluted at 0.2 mL min⁻¹. The MS spectrometer was operated in positive ionization mode over the range m/z = 50 − 1000. Capillary voltage and cone voltage were 4.5 kV and 25 V, respectively. Desolvation and source temperatures were 300 °C and 120 °C, respectively. Nitrogen was used as sheath gas at a flow rate of 35 arb units and as auxiliary gas at a flow rate of 5 arb units.
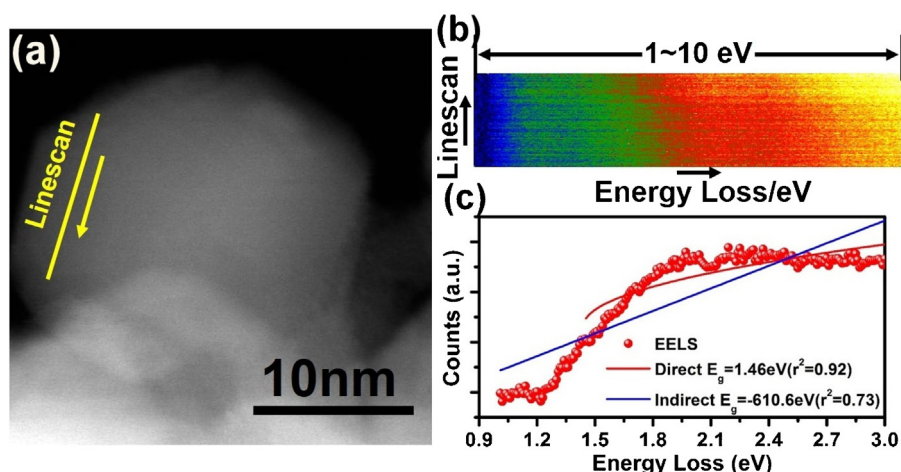
Fig. 7. HAADF image of an individual bismuth nanoparticle (a, solid line and arrow indicate the line-scanning region and direction, respectively), and a representative low-loss EELS with E_g determination (b, c).

2.3. Electron microscopy characterization and optical properties

Prior to the electron microscopy investigation, the specimen of BiOCl was dispersed in ethanol first, followed by depositing on a holey carbon film on a copper TEM grid. Both ex-situ high-resolution (HR) TEM analysis and high angle annular dark field imaging in scanning TEM (STEM-HAADF) mode were carried out for the single crystallized Bi NPs at different α-tilt angles on a FEI Tecnai F20 TEM with a field emission gun operating at 200 kV. The in-situ TEM video was also recorded at a rate of ca.10 frame/s by the software of CamStudio[TM]. Aberration-corrected HRTEM and Mono-STEM-EELS with the corresponding HAADF images were acquired on an FEI Titan S/TEM Cubed with a field emission gun operating at 300 kV. The energy resolution of Mono-STEM-EELS acquisition was 0.11 eV achieved by means of a Wien-type monochromator that is able to disperse the e^- beam over a narrow energy-selecting slit.

In order to investigate the LSPR properties of single bismuth nanoparticle, the low-loss Mono-STEM-EELS maps with binning of 900 spectra from 30×30 pixels were obtained with a scanning step of 1.2 nm and energy dispersion of 0.01 eV/channel, where each pixel was acquired for 0.05 s. To identify the LSPR absorption and E_g of as-prepared Bi NPs, the low-loss Mono-STEM-EELS spectra were extracted 2–3 nm off and in the nanoparticle's surface, respectively. To measure the volume-loss of single bismuth nanoparticle, the line-scanning low-loss Mono-STEM-EELS with 128 pixels in total were acquired with 20 ms/pixel and energy dispersion of 0.01 eV/channel. The standard power-law background subtraction has been adopted to remove the elastic peaks (zero loss peak, ZLP) in low-loss EELS. The specimen at the edge of a hole on the carbon film was selected for the Mono-STEM-EELS measurement to avoid the strong bulk plasmon signal of carbon film.

Besides, both UV–vis (200–800 nm) and NIR (800–1200 nm) absorption spectra of commercialized micro- and nano-sized bismuth particles were measured on a Varian Cary 5000 UV–vis spectrophotometer in diffuse reflectance spectroscopy (DRS) mode, using pure $BaSO_4$ as a reference.

2.4. Simulations

For studying representative geometries and comparing to Mono-STEM-EELS, the optical simulation was conducted for a sphere with the diameter of 20 nm, and a hexagonal prism with the edge length and height of 10 nm and 20 nm, respectively. The extinction spectrum is modelled by rigorously solving Maxwell's equations with the volume integral equation-fast Fourier transform method [32,33]. The optical theorem is employed to calculate the extinction cross section [34].

DFT calculations were performed with the Vienna Ab initio Simulation Package (VASP) [35]. The electron exchange and correlation were described with the generalized gradient approximation (GGA) of Perdew, Burke, and Ernzerhof (PBE), using the potentials supplied by VASP with the projected augmented wave (PAW) method. Convergence tests indicated that 150 eV was a sufficient cut-off for the pseudopotential to achieve high precision in the bismuth crystal system. The band structure was also calculated by PBE scheme within this software.

3. Results and discussion

The visible-light-induced photodegradation of RB over Bi/BiOCl catalyst prepared by photoreduction method was carried out to validate the improved photoreactivity caused by broadening the light harvesting as well as the efficient charge transfer as proved by our electron microscopy techniques. Fig. 1 shows the changes of RB concentration over Bi/BiOCl catalyst as a function of irradiation time. For comparison purposes, the degradation results over pristine BiOCl conducted under identical conditions were depicted as well. Around 92% of RB was decomposed on Bi/BiOCl catalyst compared with 78% on pristine BiOCl. Moreover, it is noteworthy that the wavelength of the characteristic absorption peak of RB solution centered at 554 nm respectively shifts to shorter wavelength of 527 nm in the presence of Bi/BiOCl compared with that of 537 nm over pristine BiOCl, showing a superior photoreactivity and the *N*-deethylation in the presence of Bi NPs. HPLC results show the chromatographic peak intensity of RB molecules (at retention time of 22.3 min) is weakened dramatically after photodegradation, and new chromatographic peaks with different retention times appear, indicating that the RB molecules were efficiently decomposed and new molecules were formed in the photosensitization process [36]. By reference to external standards, two kinds of *N*-deethylated Rhodamine products of R19 and R110 molecules were identified at retention time of 17.9 min and 2.6 min, respectively. Furthermore, as depicted in Fig. S1 (a–d, Supplementary data), five kinds of *N*-deethylated products (DER) have been evidently identified by means of LC–MS analysis, suggesting that the *N*-deethylation of RB might be a stepwise course in photosensitization process. Another model contaminant of MB was also selected to supplementary evaluate the photoreactivity because the photosensitized degradation of MB may not be involved under visible light irradiation as confirmed by the control experiment and pervious report [37]. The

results shown in Fig. S1 (e and f, Supplementary data) further suggested the boosted photocatalytic degradation and mineralization performance of MB by bismuth hybridized BiOCl catalyst under full-arc Xenon light irradiation. Under identical operation conditions, it is also interesting to find that around 30.5% of MB could still be effectively decomposed onto Bi/BiOCl catalysts driven by visible light where the BiOCl was not excited, implying that the visible-light-induced photochemical reaction rooted in the optical excitation at 1.55 − 3.1 eV of the bismuth nanoparticle might take place.

The direct synthesis of Bi/BiOCl in TEM was conducted before addressing the mechanism behind the improved photoreactivity of Bi/BiOCl catalyst by electron microscopy analysis. Stimulated by an adequate energy transfer from the electrons in an electron microscope under high vacuum, as shown in Fig. 2(a–e) and in-situ TEM video (Supplementary data), the nucleation, growth and coalescence of Bi NPs onto BiOCl can be observed in real time [29]. The surface of BiOCl was clean and smooth initially, however, with a prolonged e− beam irradiation, the nucleation of a few Bi NPs can be found throughout the entire irradiated region, followed by a multiple coalescence among nanoparticles. The particle morphology continuously changed until Bi NPs with 2D-projected hexagonal shape were observed. In addition, the atomic step has also been observed on the (110) surface of bismuth nanoparticle during the e− beam induced growing process (Fig. 2f), which has been considered to play a significant role in the enhanced photocatalytic performance [38]. Unfortunately, an ex-situ TEM investigation as shown in Fig. 3, shows that the surface reconstruction of the as-grown Bi NPs cannot be avoided after exposing in air and room temperature. The oxidation kinetics of Bi NPs is thermodynamically spontaneous from 200 to 1600 K and strongly dependent on the temperature [39], but nevertheless, no apparent surface oxidation is observed from the HRTEM images of individual bismuth nanoparticle, indicating the relative chemical stability and potential application as a heterogeneous Bi NPs hybridized photocatalyst.

The UV–vis absorption spectroscopy has been widely adopted to examine the optical absorption properties of crystalline semiconductors. As shown in Fig. S2 (Supplementary data), two principal absorption bands were noticed in UV–vis regions for pristine bismuth specimen, which are in agreement with many previous studies [12–16]. However the UV–vis cannot distinguish the optical absorptions from the surface and bulk, due to its lack of spatial resolution for the targeted specimen. An e− beam could impact and image a sample with a much higher resolution than that achieved in optical microscopy. But more importantly, different from excitation of plasmons by photons, plasmons also can be directly excited by incident e− beam. When the e− beam incident from the top that behaves like a Hertzian dipole source oriented vertically at the impinging point on the sample surface, the dipole source will produce broadband evanescent wave and thus surface or local plasmons can be excited [40]. Thanks to the recent development of electron monochromator which enables the energy resolution even higher than 100 meV, monochromated EELS is becoming a very powerful electron microscopy technique that is capable of probing the optical modes of LSPR in nanostructured materials [41–44].

As depicted in Fig. 4, the low-loss Mono-STEM-EELS spectra along with Gaussian fittings, extracted from the surface-loss EELS of a single bismuth nanoparticle, clearly show the energy loss peak at 5.5 eV (equivalent to 225 nm). The longer e− beam exposure time led to the further growth of Bi NPs, and the extinction cross-section was in proportion to the 3rd power of particle size according to the Mie theory [45]. Thereby, surface energy loss at 5.5 eV was noticeable in EELS signal, and was progressively intensified as the e− beam irradiations increased to 40 min.

Low-loss Mono-STEM-EELS maps were obtained by scanning probe in x-y direction across the region of interests, and the loca-

tions with strong EELS response (corresponds to the high brightness in the map) indicate their strongly active optical modes. As shown in Fig. 5, the Mono-STEM-EELS maps with different energies of Bi/BiOCl catalyst prepared under e− beam irradiation for 40 min, further approve that the energy losses for surface plasmons is largely spread over 5–7 eV. Additionally, the surface-loss EELS extracted at 5.5 eV was also found to gradually expand from the specimen's surface to the vacuum as the growth of Bi NPs took place.

The optical extinction spectra have been simulated and further compared with the surface-loss EELS results. It is reasonable to believe that the as-prepared single bismuth nanoparticle may have the hexagonal prism 3D structure in the light of HRTEM images (as depicted in Fig. 22e and Fig. 3) and HAADF images taken with different α-tilt degrees (Fig. S3, Supplementary data). For the purposes of simplification, the simulation was conducted assuming a sphere with diameter of 20 nm, or a hexagonal prism with edge length and height of 10 nm and 20 nm, respectively.

For a single bismuth nanoparticle with a spherical or hexagonal morphology, as depicted in Fig. 6, a pronounced excitation peak at ca. 260 nm can be observed, which suggests a local surface plasmon resonance and agrees with the peak in the Mono-STEM-EELS results. The electric field distribution around 5.5 eV suggests the surface plasmonic absorption peak is mainly dominated by the fundamental dipolar mode. The peak shifting between the optical extinction and experimental Mono-STEM-EELS spectra can be understood by the following two aspects: (1) the refractive index adopted in the simulation may deviate from that in the real sample [33]; (2) The e− beam can be regarded as a dipole source that is different from plane waves used in extinction spectra calculation. Under a dipole source (e− beam) incidence, the high-order mode of bismuth scatters [46].

The low-loss Mono-STEM-EELS signals (i.e. from the bulk of a single bismuth nanoparticle), as shown in Fig. 7(a, b), suggested a much smaller energy loss at around 1.4 eV that was not detected noticeably in the surface-loss EELS (Fig. S4, Supplementary data). The E_g in bismuth nanoparticle could be assigned to the significant quantum confinement [9]. The energy loss near the band edge for a crystalline semiconductor in EELS spectra can be described by the following equation,

$$I = I_0 + K(E - E_g)^n \qquad (1)$$

where I and I_0 are the relative intensity (measured in counts) in EELS and the corresponding baseline, respectively. E, E_g, K and n are the low energy loss (eV), band gap (eV), proportionality constant, and exponent which indicates the characteristic of transition type in a semiconductor (n = 0.5, direct transition; n = 1.5, indirect transition), respectively [47]. As depicted in Fig. 7(c), when an indirect band transition model was adopted, absurd E_g value (indirect E_g = −610.6 eV) with quite low fitting coefficient (r^2 = 0.73) was obtained. However, reasonable E_g value (direct E_g = 1.46 eV) with relatively high fitting coefficient (r^2 = 0.92) was found if we used the parabolic equation for direct E_g determination. This indicates the nature of direct band transition in bismuth, which is also in consistent with the DFT calculation (Fig. S5, Supplementary data) and previous reports [9]. Since the fitted E_g is strongly replied on the energy window selected [48], the E_g value of e− beam produced single bismuth nanoparticle has been determined statistically at 1.42 ± 0.08 eV by selecting various power-law based EELS background subtractions which take account of the zero-loss contribution (Fig. S6, Fig. S7 and Table S1, Supplementary data). Moreover, supplementary NIR absorption spectrum of commercial bismuth nanoparticles with average size of 40 nm shows the E_g value of ca. 1.58 eV (Fig. S8, Supplementary data), suggesting a nice agreement with the results obtained via EELS analysis as well. Additionally, based on the line-scanning low-loss EELS results, the
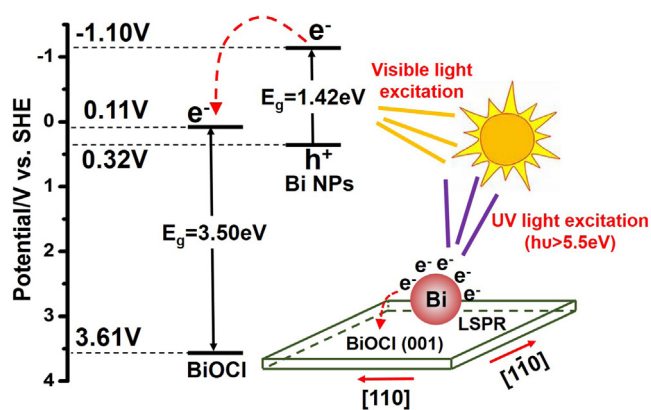
Fig. 8. Schematic illustration of the energy band diagram and possible flow of charge carriers at the interface of Bi/BiOCl driven by visible and UV light.

computed value for thickness of an individual bismuth nanoparticle was only ca. 6 nm (Fig. S9, Supplementary data), but the direct transition in Bi NPs with much smaller thickness could facilitate the high efficiency by harvesting entire visible light irradiations.

The band edge potential of bismuth can be calculated by Mulliken electronegativity theory,

$$E_{CB} = X - E_c - 1/2E_g \qquad (2)$$

where X is the absolute electronegativity of the semiconductor, E_c the energy of free electrons on hydrogen scale (4.5 eV) and E_g the band gap of the semiconductor [49].The band edge potentials of CB and VB have been theoretically speculated at -1.1 V and 0.32 V with respect to the standard hydrogen electrode (SHE) potential, respectively (Table S2, Supplementary data). Therefore the Bi/BiOCl interface might be considered as a typical staggered gap (type II) band alignment as shown in Fig. 8. Owning to the over-potential between the CB edges of Bi NPs and BiOCl as portrayed, the CB of BiOCl may favorably accept the visible-light-excited electrons from the CB of photosensitizer (bismuth) that is able to harvest the entire visible light energy, indicating that the photogenerated carries in both Bi NPs and BiOCl semiconductor could be separated. Because of the extremely low VB edge potential of Bi NPs (0.32 V vs. SHE), the photogenerated holes in bismuth are incapable of directly oxidizing adsorbed hydroxyl groups to produce hydroxyl radicals (2.7 V vs. SHE) that are considered as an essential active species during the photodegradation process. Therefore the hydroxyl radicals might be generated through the multistep reduction of dissolved oxygen in aqueous solution by photoexcited electrons (i.e. the photosensitization process) [50]. Under UV light exposure, additionally, hot electrons could be generated from the surface of Bi NPs through the non-radiative decay of localized surface plasmons and immigrated to the CB of BiOCl.

4. Conclusions

In conclusion, advanced (in-situ) electron microscopy was used to understand the mechanism of enhanced photosensitization decomposition of RB molecules over Bi/BiOCl catalyst driven by visible light. The e$^-$ beam induced nucleation, growth and coalescence of Bi NPs onto BiOCl (i.e. the formation of Bi/BiOCl hybridized photocatalyst) was witnessed directly in a TEM. After 2 h air exposure at room temperature, the surface reconstruction and relatively high chemical stability of the as-grown Bi NPs were noticed in ex-situ TEM investigation. The measured energy loss at 5.5 eV from the surface of bismuth nanoparticle caused by the LSPR effect has been confirmed by both Mono-STEM-EELS and theoretical simulation. The direct E_g at 1.42 ± 0.08 eV of single bismuth nanoparticle shows

the harvesting capability of Bi/BiOCl catalyst in the entire visible light region. A typical interfacial energy band structure of staggered gap (type II) could be generated due to the semiconducting property of Bi NPs with matched band edge positions with BiOCl, which facilitates the photoreactivity under visible light irradiation. We believe that these findings should pave the way to the insightful understanding of the enhanced photoreactivity onto Bi/BiOCl and others bismuth-hybridized photocatalysts.

Appendix A. Supplementary data

Supplementary data associated with this article can be found, in the online version, at http://dx.doi.org/10.1016/j.apcatb.2016.08.049.

References

[1] R. Asahi, T. Morikawa, T. Ohwaki, K. Aoki, Y. Taga, Science 293 (2001) 269–271.
[2] Z. Zou, J. Ye, K. Sayama, H. Arakawa, Nature 414 (2001) 625–627.
[3] A. Kudo, Y. Misekia, Chem. Soc. Rev. 38 (2009) 253–278.
[4] X.B. Chen, L. Liu, P.Y. Yu, S.S. Mao, Science 331 (2011) 746–750.
[5] S. Linic, P. Christopher, D.B. Ingram, Nat. Mater. 10 (2011) 911–921.
[6] Q.J. Xiang, J.G. Yu, M. Jaroniec, Chem. Soc. Rev. 41 (2012) 782–796.
[7] D.M. Schultz, T.P. Yoon, Science 343 (2014) 985–993.
[8] J. Liu, Y. Liu, N.Y. Liu, Y.Z. Han, X. Zhang, H. Huang, Y. Lifshitz, S.T. Lee, J. Zhong, Z.K. Kang, Science 347 (2015) 970–974.
[9] M.R. Black, Y.M. Lin, S.B. Cronin, O. Rabin, M.S. Dresselhaus, Phy. Rev. B 65 (2002) 195417.
[10] M. Gutiérrez, A. Henglein, J. Phys. Chem. 100 (1996) 7656–7661.
[11] F.L. Xia, X.Y. Xu, X.C. Li, L. Zhang, L. Zhang, H.X. Qiu, W. Wang, Y. Liu, J.P. Gao, Ind. Eng. Chem. Res. 53 (2014) 10576–10582.
[12] F. Qin, R.M. Wang, G.F. Li, F. Tian, H.P. Zhao, R. Chen, Catal. Commun. 42 (2013) 14–19.
[13] F. Dong, T. Xiong, Y.J. Sun, Z.W. Zhao, Y. Zhou, X. Feng, Z.B. Wu, Chem. Commun. 50 (2014) 10386–10389.
[14] Z. Wang, C.L. Jiang, R. Huang, H. Peng, X.D. Tang, J. Phys. Chem. C 118 (2014) 1155–1160.
[15] F. Dong, T. Xiong, Y.J. Sun, Z.W. Zhao, Y. Zhou, X. Feng, Z.B. Wu, Chem. Commun. 50 (2014) 10386–10389.
[16] J. Zhao, Q.F. Han, J.W. Zhu, X.D. Wu, X. Wang, Nanoscale 6 (2014) 10062–10070.
[17] S.X. Weng, B.B. Chen, L.Y. Xie, Z.Y. Zheng, P. Liu, J. Mater. Chem. A 1 (2013) 3068–3075.
[18] F. Dong, Q.Y. Li, Y.J. Sun, W.K. Ho, ACS Catal. 4 (2014) 4341–4350.
[19] Y. Yu, C.Y. Cao, H. Liu, P. Lia, F.F. Wei, Y. Jiang, W.G. Song, J. Mater. Chem. A 2 (2014) 1677–1681.
[20] J.J. Hu, G.Q. Xu, J.W. Wang, J. Lv, X.Y. Zhang, Z.X. Zheng, T. Xie, Y.C. Wu, New J. Chem. 38 (2014) 4913–4921.
[21] X.M. Zhang, G.B. Ji, Y.S. Liu, X.G. Zhou, Y. Zhu, D.N. Shi, P. Zhang, X.Z. Cao, B.Y. Wang, Phys. Chem. Chem. Phys. 17 (2015) 8078–8086.
[22] Y.J. Sun, Z.W. Zhao, F. Dong, W. Zhang, Phys. Chem. Chem. Phys. 17 (2015) 10383–10390.
[23] D. Velasco-Arias, I. Zumeta-Dubé, D. Díaz, P. Santiago-Jacinto, V.F. Ruiz-Ruiz, S.E. Castillo-Blum, L. Rendoń, J. Phys. Chem. C 116 (2012) 14717–14721.
[24] C.C. Feng, D.H. Wang, B.J. Jin, Z.B. Jiao, RSC Adv. 5 (2015) 75947–75952.
[25] D.S. Su, B. Zhang, R. Schloegl, Chem. Rev. 115 (2015) 2818–2882.
[26] H.G. Liao, K.Y. Niu, H.M. Zheng, Chem. Commun. 49 (2013) 11720–11727.

[27] L.Z. Li, J.R. Jokisaari, X.Q. Pan, MRS Bull. 40 (2015) 53–61.
[28] P. Specht, J.C. Ho, X. Xu, R. Armitage, E.R. Weber, R. Erni, C. Kisielowski, Solid State Commun. 135 (2005) 340–344.
[29] X.F. Chang, S.B. Wang, Q. Qi, M.A. Gondal, S.G. Rashid, S. Gao, D.Y. Yang, K. Shen, Q.Y. Xu, P. Wang, Dalton Trans. 44 (2015) 15888–15896.
[30] X.F. Chang, S.B. Wang, Q. Qi, M.A. Gondal, S.G. Rashid, D.Y. Yang, M.A. Dastageer, K. Shen, Q.Y. Xu, P. Wang, Appl. Catal. B: Environ. 176 (2015) 201–211.
[31] K. Yu, S.G. Yang, H. He, C. Sun, C.G. Gu, Y.M. Ju, J. Phys. Chem. A 113 (2009) 10024–10032.
[32] W.E.I. Sha, W.CH. Choy, Y.P.P. Chen, W.C. Chew, Opt. Express 19 (2011) 15908–15918.
[33] J.M. McMahon, G.C. Schatz, S.K. Gray, Phys. Chem. Chem. Phys. 15 (2003) 5415–5423.
[34] W.C. Chew, L.J. Jiang, S. Sun, W.E.I. Sha, Q.I. Dai, M. Fallahpour, Y.M. Wu, Numerical modeling in antenna engineering, in: Z.N. Chen (Ed.), Handbook of Antenna Technologies, Springer, 2015, pp. 1–71.
[35] G. Kresse, J. Furthmuller, Comput. Mater. Sci. 6 (1996) 15–50.
[36] Q. Wang, C.C. Chen, D. Zhao, W. Ma, J.C. Zhao, Langmuir 24 (2008) 7338–7345.
[37] X.F. Chang, M.A. Gondal, A.A. Al-Saadi, M.A. Ali, H.F. Shen, Q. Zhou, J. Zhang, M.P. Du, Y.S. Liu, G.B. Ji, J. Colloid Interface Sci. 377 (2012) 291–298.
[38] M. Matsukawa, R. Ishikawa, T. Hisatomi, Y. Moriya, N. Shibata, J. Kubota, Y. Ikuhara, K. Domen, Nano. Lett. 14 (2014) 1038–1041.
[39] J.Y. Xia, M.T. Tang, C. Chen, S.M. Jin, Y.M. Chen, Trans. Nonferrous Met. Soc. China 22 (2012) 2289–2294.
[40] E.J.R. Vesseur, J. Aizpurua, T. Coenen, A. Reyes-Coronado, P.E. Batson, A. Polman, MRS Bull. 37 (2012) 752–760.
[41] J. Nelayah, M. Kociak, O. Stéphan, F.J.G. DE Abajo, M. Tencé, L. Henrard, D. Taverna, I. Pastoriza-Santos, L.M. Liz-Marzán, C. Colliex Nat. Phys. 3 (2007) 348–353.
[42] H.Y. Liang, D. Rossouw, H.G. Zhao, S.K. Cushing, H.L. Shi, A. Korinek, H.X. Xu, F. Rosei, W.Z. Wang, N.Q. Wu, G.A. Botton, D.L. Ma, J. Am. Chem. Soc. 135 (2013) 9616–9619.
[43] S. Kadkhodazadeh, J.R. de Lasson, M. Beleggia, H. Kneipp, J.B. Wagner, K. Kneipp, J. Phys. Chem. C 118 (2014) 5478–5485.
[44] M. Bosman, E.Y. Ye, S.F. Tan, C.A. Nijhuis, J.K.W. Yang, R. Marty, A. Mlay, Sci. Rep. 3 (2013) 1312.
[45] M. Hu, J.Y. Chen, Z.Y. Li, L. Au, G.V. Hartland, X.D. Li, M. Marquez, Y.N. Xia, Chem. Soc. Rev. 35 (2006) 1084–1094.
[46] L. Novotny, B. Hecht, Principles of Nano-Optics, Cambridge University Press, 2006.
[47] B. Rafferty, L.M. Brown, Phy. Rev. B 58 (1998) 10326–10337.
[48] R. Erni, N.D. Browning, Ultramicroscopy 104 (2005) 176–192.
[49] S. Li, L.B. Hou, L.J. Zhang, L.P. Chen, Y.H. Lin, D.J. Wang, T.F. Xie, J. Mater. Chem. A 3 (2015) 17820–17826.
[50] S.C. Yan, Z.S. Li, Z.G. Zou, Langmuir 26 (2010) 3894–3901.